Ocean Engineering 233 (2021) 109210

Contents lists available at ScienceDirect

Ocean Engineering

journal homepage: www.elsevier.com/locate/oceaneng

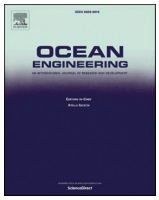

Numerical study of closed rigid fish cages in waves and comparison with experimental data

Biao Su [a,*], Andrei Tsarau [a], Per Christian Endresen [a], David Kristiansen [b], Pål Furset Lader [b]

[a] SINTEF Ocean, Trondheim, Norway
[b] Department of Marine Technology, NTNU, Trondheim, Norway

ARTICLE INFO

Keywords:
Marine aquaculture
Closed fish cage
Wave-induced response
Sloshing
Numerical modelling

ABSTRACT

Closed fish cages have gained increased interest in marine aquaculture. However, knowledge on the seakeeping behaviour of a floating closed cage and the influence of the contained water inside the cage are still limited. In this paper, a coupled numerical model is developed for the simulation of closed rigid cages in waves. Numerical studies are conducted both in the frequency domain and in the time domain, and compared with scaled physical experiments. Special attention has been drawn to the coupling effects of sloshing on cage response and the resulting mooring line forces. The comparative analyses show that sloshing of the contained water has large influence on the coupled surge and pitch motions of the cage. Sloshing is also found to have significant effect on the mean-drift forces in regular waves. In the tested/simulated irregular waves, the mooring forces are found to be dominated by the slow-drift motions, which indicates that the slowly-varying wave drift forces need to be considered in the design of the mooring system for a floating closed cage.

1. Introduction

Fish farming in floating closed cages has gained increased interest in recent years as a strategy to mitigate the problems with sea lice and the negative environmental impact, which are often associated with the open net cage systems that are widely used for sea-based production of Atlantic salmon (*Salmo salar*). The existing concepts of closed fish cages can be categorised as flexible membrane structures (fabric), semi-flexible structures (glass fibre) and rigid structures (steel or concrete), based on the construction materials being used and to what degree the cage can deform (Kristiansen et al., 2018a). From a marine hydrodynamics perspective, a closed cage represents a large volume structure filled with liquid. Ocean waves may excite free-surface oscillation of the contained water inside the cage causing sloshing, which is a complex phenomenon with relevance for many applications (Faltinsen and Timokha, 2009). The coupling effects of internal hydrodynamics on cage response and structural deformation, are important design considerations for floating closed cages. However, knowledge on and experience with these problems are quite limited, as sea-based fish farming in closed cages is still a novel concept.

Solaas et al. (1993) presented some important design parameters for closed flexible cages which are typically made of coated fabric. The flexible nature of these structures implies that hydroelasticity is important to consider in the marine environment (Løland, 1994). A study of drag forces and associated deformations of closed flexible cages was presented in Lader et al. (2015) and Strand et al. (2016), followed up by an experimental study on the wave-induced responses of the same closed flexible structure (Lader et al., 2017). A combined structural and hydrodynamic model was developed by Kristiansen et al. (2018b) to study the drainage and collapse of a closed flexible cage under specific operational conditions. A linear model of two-dimensional closed flexible cage in waves was developed by Strand and Faltinsen (2019) to investigate the coupling effects of sloshing on cage response and structural deformation. This model was further developed for the analysis of semi-flexible cages, including the effect of bending stiffness (Strand and Faltinsen, 2020). Kristiansen et al. (2018a) presented a dedicated experimental study of cylindrical closed rigid cages in regular waves and comparison with numerical simulations using linear potential theory in the frequency domain. Sloshing of the contained water was shown to have large influence on the coupled surge and pitch motions of the cage. Tan et al. (2019) used a single-dominant multi-modal method for the simulation of sloshing and coupled rigid body motions of a cylindrical closed cage in regular waves. It was found that the multi-modal method was able to model the swirling waves inside the cage, which could lead

* Corresponding author.
E-mail address: biao.su@sintef.no (B. Su).

https://doi.org/10.1016/j.oceaneng.2021.109210
Received 10 January 2021; Received in revised form 22 April 2021; Accepted 19 May 2021
Available online 28 May 2021

to violent cage motions even in the direction perpendicular to the incident waves. Liang et al. (2020) used a fully nonlinear time-domain harmonic polynomial cell (HPC) method (Shao and Faltinsen, 2014) to study the liquid sloshing problem in a circular cylindrical tank under periodic and transient excitations. The sloshing response in terms of free-surface elevation as well as hydrodynamic force and moments were evaluated and compared with analytical predictions from the weakly nonlinear multi-modal theory. In general, good agreement was found. Tsarau et al. (2021) presented experimental and numerical studies of a circular cylindrical tank filled with water and subjected to forced oscillations. A weakly nonlinear multi-modal method (Faltinsen and Timokha, 2009) was shown to be able to model both the planar and swirling waves with similar amplitudes to the experiments. Sloshing experiments with a rotating liquid were also conducted, and the results showed that the internal flows might significantly modify the sloshing regimes observed in the non-rotating liquid.

As a continuation of the previous work (Kristiansen et al., 2018a), this paper presents an integrated numerical model for analysing the seakeeping behaviour of closed rigid cages and the mooring forces in regular and irregular waves. Numerical studies are conducted both in the frequency domain and in the time domain, and compared with scaled physical experiments. The time-domain simulation enables the implementation of nonlinear hydrodynamic models and offers the possibility for a complete system analysis (e.g. cage response, structural deformation, moorings and fish behaviour) that most of the existing simulation codes do not provide. A model for slowly-varying wave drift forces, which have great importance in the design of the mooring system for floating large volume structures, is implemented. Sloshing of the contained water inside the cage is modelled based on the weakly nonlinear multi-modal method (Faltinsen and Timokha, 2009). The coupling effects of sloshing on cage response and the resulting mooring line forces are investigated.

2. Materials and methods

2.1. WAMIT

WAMIT is a state-of-the-art simulation code (distributed and licenced by WAMIT Inc., Massachusetts, USA) for analysing wave interactions with floating or submerged marine structures. The wave-induced response of a three-dimensional body in waves is simulated in the frequency domain, by evaluating the hydrodynamic pressure and forces on the body surface, as well as the fluid velocities. The flow is assumed to be potential, free of separation or lifting effects, and the linearization of the problem permits the decomposition of the velocity potential into the radiation and diffraction components. In the present study, the so-called "low-order" method is used, where the geometry of the body is represented by an ensemble of flat quadrilateral panels and the solutions for the velocity potential are approximated by piecewise constant values on each panel (www.wamit.com/manual.htm).

WAMIT provides the option to analyse the linear hydrodynamic parameters for a fluid inside an oscillatory tank, or to analyse the coupled problem where one or more tanks are placed within the interior of the body, including the dynamic coupling. This option is utilized in the present study to simulate the effect of the contained water with a free surface inside the closed cage. The tank geometry is defined in the same manner as for the exterior surface of the cage, using the "low-order" method. The solution for the velocity potential in the tank is computed simultaneously with the velocity potential in the exterior fluid domain outside the cage, using an extended linear system which includes all of the fluid domains.

2.2. The FhSim framework

FhSim is a software platform and framework for mathematical modelling and numerical simulation, with a focus on applications within fisheries and aquaculture (Reite et al., 2014; Su et al., 2019). It has been under continuous development at SINTEF Ocean since 2006, which features a large collection of mathematical models for time-domain simulations based on ordinary differential equations (ODEs). Model development in FhSim is modular, where complex systems are modelled as interconnected sub-models. In the present study, new sub-models are implemented in FhSim for the simulation of closed rigid cages and sloshing, which will be described in Sections 2.3 and 2.4. In the following, the existing FhSim sub-models for the simulation of waves and mooring lines are described in brief.

2.2.1. FhSim sub-model for the simulation of waves

FhSim contains implementations of sea environment models simulating water current and wave fields, and a generalized interface for other sub-models to query about environmental features, such as sea depth, current velocity, wave elevation and wave induced particle velocity at a specified point in the water volume. The implemented wave model supports both Eulerian and Lagrangian linear wave theories and realization of JONSWAP and ISSC wave spectra based on the superposition principle. The generated wave field is, in general, assumed to be undisturbed by other sub-models. However, wave radiation and diffraction (Faltinsen, 1993) can be considered in other sub-models (see e.g. in Section 2.3) for the calculation of wave-induced forces.

2.2.2. FhSim sub-model for the simulation of mooring lines

A generic cable model in FhSim is used for the simulation of mooring lines which are attached to other sub-models (e.g. a fish cage) or a fixed point in space (e.g. an anchor point). The cable model is essentially a collection of 6 degrees-of-freedom (DOF) rigid bar elements which are connected with axial and angular constraints. The constraints are regularized through an elastic version of the Baumgarte stabilization method (Baumgarte, 1972). In effect the rigid bar elements can be thought of as connected with axial and angular springs like a traditional spring-mass-damper model, but without some of the numerical instability problems associated with high stiffness. The behaviour of the springs is regularized with three parameters: α, β and ε, where α is the damping factor, β controls the rate at which the constraint seeks towards equilibrium, and ε is the constraint compliance. The effective spring stiffness is a combination of β, ε, and the mathematical formulation of the constraint function. For the axial spring the effective stiffness is $(\beta^2/\varepsilon)\cdot EA/L$, where E is the Young's modulus of the material, A is the element's cross-sectional area, and L is the element's length. For the bending angular spring the effective stiffness is $(\beta^2/\varepsilon)\cdot \leq EI/L$, where I is the element's second moments of area for bending. For the torsional angular spring the effective stiffness is $(\beta^2/\varepsilon)\cdot GJ/L$, where G is the shear modulus of the material, and J is the element's second moments of area for torsion.

The mooring lines are subject to gravity, buoyancy, hydrodynamic and viscous forces, and forces exerted by other sub-models attached to them. These forces are computed separately for each element comprising the cable, as well as the constraint equations providing desired structural properties for modelling the dynamic response. The cable model has been used for the simulation of a full aquaculture net-cage system in waves and current, and validated through comparison with experimental data (Endresen et al., 2014). A thorough description of the theoretical and mathematical background for the cable model can be found in Johansen (2007).

2.3. Modelling of closed rigid cages

The 6DOF motions (denoted by η_i, $i = 1, \ldots, 6$) of a floating closed rigid cage are modelled in FhSim by Cummins' equation (Cummins, 1962) in time domain:

$$\sum_{j=1}^{6}\left[\left(M_{ij}+A_{ij}(\infty)\right)\ddot{\eta}_j(t)+\int_0^t K_{ij}(t-\tau)\dot{\eta}_j(\tau)d\tau+C_{ij}\eta_j(t)\right]=F_i^{Sum}(t) \tag{1}$$

where $M_{ij}$is the component of the generalized mass matrix, $A_{ij}(\infty)$ is the added mass coefficient at infinity frequency, K_{ij} is the impulse response function representing the fluid memory effects, C_{ij} is the hydrostatic restoring coefficient, and $F_i^{Sum}(t)$ represents the sum of wave excitation forces, slow-drift forces, nonlinear viscous damping, mooring forces, and forces induced by the contained water. Note that all the forces and coefficients are defined with respect to the cage-fixed coordinate system.

In the present study, the added mass, damping, and hydrostatic restoring coefficients are obtained from the frequency-domain calculations in WAMIT (without internal tank) for a range of frequencies. The frequency-domain data are also used for a state-space approximation of the convolution term of Cummins' equation and calculation of the wave excitation and slow-drift forces.

2.3.1. State-space approximation of the radiation forces associated with fluid memory effects

The convolution term of Cummins' equation can be approximated by a linear state-space model (Kristiansen and Egeland, 2003; Fossen, 2005):

$$\mu_{ij}(t)=\int_0^t K_{ij}(t-\tau)\dot{\eta}_j(\tau)d\tau \tag{2}$$

$$\dot{\boldsymbol{\chi}}_{ij}(t)=\mathbf{A}_{ij}^{'}\boldsymbol{\chi}_{ij}(t)+\mathbf{B}_{ij}^{'}\dot{\eta}_j(t) \tag{3}$$

$$\mu_{ij}(t)=\mathbf{C}_{ij}^{'}\boldsymbol{\chi}_{ij}(t)+\mathbf{D}_{ij}^{'}\dot{\eta}_j(t) \tag{4}$$

where $\mu_{ij}(t)$ is the output of the state-space model that approximates the impulse response function in DOF i to an impulse velocity in DOF j, $\boldsymbol{\chi}_{ij}(t)$ is the state vector of the state-space model, $\mathbf{A}_{ij}^{'}$, $\mathbf{B}_{ij}^{'}$, $\mathbf{C}_{ij}^{'}$, and $\mathbf{D}_{ij}^{'}$ are the parametric system matrices. As compared with the direct computation of the convolution integral, the state-space approximation has advantages in terms of the computation speed, which can improve up to two orders of magnitude depending on the number of DOFs considered (Taghipour et al., 2008).

In the present study, the vector fitting system identification method (Gustavsen and Semlyen, 1999; Gustavsen, 2006) is used to select the system matrices $\mathbf{A}_{ij}^{'}$, $\mathbf{B}_{ij}^{'}$, $\mathbf{C}_{ij}^{'}$, and $\mathbf{D}_{ij}^{'}$ for each DOF combination ($i = 1, \ldots, 6$; $j = 1, \ldots, 6$) based on the calculated added mass and damping coefficients for a range of frequencies. A thorough description of the frequency-domain identification of parametric state-space models can be found in Kristiansen (2005) and Pérez and Fossen (2008).

2.3.2. Convolution integral and state-space approximation of the excitation forces

The first-order wave excitation force in time domain can be expressed as:

$$F_i^{Exc}(t)=\int_0^t h_i^{Exc}(t-\tau)\xi^{Inc}(\tau)d\tau \tag{5}$$

where ξ^{Inc} is the incident wave elevation at the centre of the structure, and h_i^{Exc} is the impulse response function for the excitation force, which can be calculated using the inverse Fourier transform of the corresponding force coefficient in frequency domain. Similar to the radiation force, a state-space model can be used to approximate the convolution integral for the excitation force (Yu and Falnes, 1995; Taghipour et al., 2008).

In the present study, the first-order excitation forces for long-crested irregular waves are evaluated based on the superposition principle:

$$F_i^{Exc}(t)=\sum_{j=1}^{N}A_jT_j^{hi}\cos\left(\omega_jt+\varepsilon_j\right) \tag{6}$$

where N is the number of regular wave components used for the time-domain realization of JONSWAP spectrum, A_j, ω_j, and ε_j are the wave amplitude, circular frequency, and relative phase angle of wave component number j, and T_i^{hi} is the transfer function of the wave excitation force for DOF i which can be obtained from the first-order frequency-domain solution for each regular wave component.

2.3.3. Newman's approximation of the slow-drift forces

For a moored large volume structure, the restoring provided by the mooring lines leads to large resonance periods of the horizontal motions, and slow-drift motions can occur in the horizontal plane. In the present study, the Newman's approximation (Newman, 1974) is used to calculate the slowly-varying wave drift forces for long-crested irregular waves considering the second-order difference-frequency effects:

$$F_i^{SD}(t)=\sum_{j=1}^{N}\sum_{k=1}^{N}A_jA_k\sqrt{T_j^{di}T_k^{di}}\cos\left[\left(\omega_k-\omega_j\right)t+\left(\varepsilon_k-\varepsilon_j\right)\right] \tag{7}$$

where T_j^{di} is the transfer function of the mean-drift force for DOF i, which depends only on the first-order frequency-domain solution for each regular wave component. For example, in WAMIT the mean-drift force can be evaluated based on either pressure integration or momentum conservation principle, without calculation of the second-order velocity potential.

This expression is also valid for regular wave, i.e. these is only one wave component, in this case the calculated slow-drift force is equal to the constant mean-drift force.

2.4. Modelling of sloshing

A weakly nonlinear multi-modal method (Faltinsen and Timokha, 2009), using the Fourier (modal) approximate solution of the free-surface elevation with time-dependent coefficients, is implemented in FhSim to simulate sloshing of the contained water inside a closed rigid cage. The cage is considered to be a vertical, cylindrical tank of radius R, which is partially filled with an inviscid incompressible liquid of depth h.

2.4.1. Natural sloshing modes

Following modal theory, the free-surface elevation ξ inside the cage is expanded as a series in terms of so-called natural sloshing modes $\chi_{m,i,k}(x,y)$:

$$\xi(x,y,t)=\sum_{m,i,k}\beta_{m,i,k}(t)\chi_{m,i,k}(x,y) \tag{8}$$

where $\beta_{m,i,k}$ are the generalized coordinates for liquid motion, which are infinite in number, and the sum goes over all β. According to linear potential flow theory, the natural modes for an upright circular cylinder in a cylindrical coordinate system (r,θ,z) read as

$$\chi_{m,i,k}(x,y)=\chi_{m,i,k}(r\cos\theta,r\sin\theta)=\frac{J_m\left(l_{m,i}r/R\right)}{J_m\left(l_{m,i}\right)}\times\begin{cases}\cos(m\theta)\\ \sin(m\theta)\end{cases} \tag{9}$$

where J_m is the Bessel function of the first kind of order m, and $l_{m,i}$ are the nondimensional roots of the equation $J_m^{'}(l_{m,i})=0$, and index k (= 1 or 2) corresponds to the cosine or sine mode terms, respectively.

For each natural mode, the corresponding natural frequencies are

$$\sigma_{m,i}^2=\frac{g}{R}l_{m,i}\tanh\left(l_{m,i}\frac{h}{R}\right) \tag{10}$$

where g is the acceleration of gravity (9.81 m/s^2), and $m = 0, 1, 2, \ldots$; $i = 1, 2, \ldots$ are the so-called azimuthal and radial mode numbers, respectively.

2.4.2. Modal equations for prescribed tank motions

When rigid-body motions η_i are known, the following ordinary differential equations describe liquid motion in terms of the generalized coordinates

$$\ddot{\beta}_{1,j,1} + \sigma_{1,j}^2\beta_{1,j,1} + 2\sigma_{1,j}\delta_{1,j}\dot{\beta}_{1,j} + B_{1,j,1} = -P_j\left[\ddot{\eta}_1 - g\eta_5 - S_j\ddot{\eta}_5\right], \tag{11}$$

$$\ddot{\beta}_{1,j,2} + \sigma_{1,j}^2\beta_{1,j,2} + 2\sigma_{1,j}\delta_{1,j}\dot{\beta}_{1,j} + B_{1,j,2} = -P_j\left[\ddot{\eta}_2 + g\eta_4 + S_j\ddot{\eta}_4\right], \tag{12}$$

$$\ddot{\beta}_{2,j,k} + \sigma_{2,j}^2\beta_{2,j,k} + 2\sigma_{2,j}\delta_{2,j}\dot{\beta}_{2,j} + B_{2,j,k} = 0,\ k = 1, 2 \tag{13}$$

$$\ddot{\beta}_{0,j,1} + \sigma_{0,j}^2\beta_{0,j,1} + 2\sigma_{0,j}\delta_{0,j}\dot{\beta}_{0,j,1} + B_{0,j,1} = 0, \tag{14}$$

$$P_j = \frac{2l_{1,j}\tanh\left(l_{1,j}h/R\right)}{l_{1,j}^2 - 1}, \tag{15}$$

$$S_j = \frac{2R\tanh\left(l_{1,j}h/2R\right)}{l_{1,j}} \tag{16}$$

where $j = 1, 2, \ldots \le I_r$ (number of the radial modes, here 2), $m = 0, 1, 2$ – the only azimuthal numbers that have a nonzero contribution, and index k (= 1 or 2) corresponds to the cosine or sine mode terms, respectively, and $B_{i,j,k}$ are the nonlinear terms defined below. The linear damping term (with modal damping ratios denoted by $\delta_{m,j}$) is introduced artificially in order to achieve steady-state solutions of the modal equations. Possible values of $\delta_{m,j}$ are discussed in Section 2.4.3.

The nonlinear terms in the above modal equations for tank excitation frequencies close to $\sigma_{1,1}$ was derived by Lukovsky (1990). Following Faltinsen and Timokha (2009), we use the traditional notations, $p_1 = \beta_{1,1,1}$, $r_1 = \beta_{1,1,2}$, $p_0 = \beta_{0,1,1}$, $p_2 = \beta_{2,1,1}$, $r_2 = \beta_{2,1,2}$, such that the nonlinear terms read:

$$\begin{aligned} B_{1,1,1} = {} & \frac{d_1}{R^2}p_1\left(p_1\ddot{p}_1 + \dot{p}_1^2 + r_1\ddot{r}_1 + \dot{r}_1^2\right) + \frac{d_2}{R^2}\left(r_1^2\ddot{p}_1 + 2r_1\dot{r}_1\dot{p}_1 - r_1p_1\ddot{r}_1 - 2p_1\dot{r}_1^2\right) \\ & + \frac{d_3}{R}\left(p_2\ddot{p}_1 + r_2\ddot{r}_1 + \dot{r}_1\dot{r}_2 + \dot{p}_1\dot{p}_2\right) - \frac{d_4}{R}\left(p_1\ddot{p}_2 + r_1\ddot{r}_2\right) \\ & + \frac{d_5}{R}\left(p_0\ddot{p}_1 + \dot{p}_1\dot{p}_0\right) + \frac{d_6}{R}p_1\ddot{p}_0 \end{aligned} \tag{17}$$

$$\begin{aligned} B_{1,1,2} = {} & \frac{d_1}{R^2}r_1\left(r_1\ddot{r}_1 + \dot{r}_1^2 + p_1\ddot{p}_1 + \dot{p}_1^2\right) + \frac{d_2}{R^2}\left(p_1^2\ddot{p}_1 + 2p_1\dot{r}_1\dot{p}_1 - r_1p_1\ddot{p}_1 - 2r_1\dot{p}_1^2\right) \\ & - \frac{d_3}{R}\left(p_2\ddot{r}_1 + r_2\ddot{p}_1 + \dot{r}_1\dot{p}_2 - \dot{p}_1\dot{r}_2\right) + \frac{d_4}{R}\left(r_1\ddot{p}_2 - p_1\ddot{r}_2\right) \\ & + \frac{d_5}{R}\left(p_0\ddot{r}_1 + \dot{r}_1\dot{p}_0\right) + \frac{d_6}{R}r_1\ddot{p}_0 \end{aligned} \tag{18}$$

$$B_{0,1,1} = \frac{d_{10}}{R}\left(r_1\ddot{r}_1 + p_1\ddot{p}_1\right) + \frac{d_8}{R}\left(\dot{r}_1^2 + \dot{p}_1^2\right) \tag{19}$$

$$B_{2,1,1} = \frac{d_9}{R}\left(r_1\ddot{r}_1 - p_1\ddot{p}_1\right) + \frac{d_7}{R}\left(\dot{r}_1^2 - \dot{p}_1^2\right) \tag{20}$$

$$B_{2,1,2} = \frac{d_9}{R}\left(r_1\ddot{p}_1 + p_1\ddot{r}_1\right) - \frac{2d_7}{R}\dot{r}_1\dot{p}_1 \tag{21}$$

The coefficient $d_1, \ldots d_{10}$ in these nonlinear terms are tabulated by Faltinsen and Timokha (2009) for a range of h/R between 0.2 and 3.0. The presented model includes nonlinear terms only for the two primary excited modes ($(1,1,1)$ and $(1,1,2)$) and the secondary modes ($(0,1,1)$, $(2,1,1)$, $(2,1,2)$). Thus, there is no coupling between the third-order modes and higher.

2.4.3. Viscous energy dissipation

Although potential theory assumes inviscid liquid, viscous energy dissipation in the liquid can be included in the modal equations for liquid motion, as shown in the previous section. In general, there is viscous dissipation in both the boundary layers and in the bulk of the fluid. However, bulk damping is often considered small relative to boundary-layer damping and is usually neglected (Faltinsen and Timokha, 2009). Royon-Lebeaud et al. (2007) have shown that for dissipation at the boundaries of a circular-cylindrical tank, the damping ratios can be estimated using the following analytical expression:

$$\begin{aligned} \delta_{m,n} = {} & \frac{1}{2R}\left(\frac{\nu}{2\sigma_{m,n}}\right)^{1/2}\left[\frac{2l_{m,n}}{\sinh\left(2l_{m,n}h/R\right)} + \frac{2l_{m,n}\cosh^2\left(l_{m,n}h/R\right)}{\sinh\left(2l_{m,n}h/R\right)} + \frac{1 + \left(m/l_{m,n}\right)^2}{1 - \left(m/l_{m,n}\right)^2}\right. \\ & \left. - \frac{2l_{m,n}h/R}{\sinh\left(2l_{m,n}h/R\right)}\right] \end{aligned} \tag{22}$$

where ν is the kinematic viscosity of the liquid. Note, however, that Royon-Lebeaud et al. (2007) used this expression for smooth-wall cylinders. Aquaculture cages for salmon production may have nonsmooth walls (e.g. due to biofouling) and are typically equipped with pipe systems for generating a liquid flow inside the cage, which may contribute to the viscous damping.

2.4.4. Hydrodynamic force

The total hydrodynamic force on the cage can be expressed via the generalized coordinates following Faltinsen and Timokha (2009):

$$F_{\eta_1} = \pi\rho R^2 h\left(g\eta_5 - \ddot{\eta}_1 + \frac{1}{2}h\ddot{\eta}_5\right) - \sum_{j=1}^{I_r}\frac{\pi\rho R^3}{l_{1,j}^2}\ddot{\beta}_{1,j,1} \tag{23}$$

$$F_{\eta_2} = \pi\rho R^2 h\left(-g\eta_4 - \ddot{\eta}_2 - \frac{1}{2}h\ddot{\eta}_4\right) - \sum_{j=1}^{I_r}\frac{\pi\rho R^3}{l_{1,j}^2}\ddot{\beta}_{1,j,2} \tag{24}$$

$$F_{\eta_3} = -\pi\rho R^2 h\left(g + \ddot{\eta}_3\right) \tag{25}$$

where ρ is the liquid density. Likewise, the hydrodynamic moment can also be expressed via the generalized coordinates. For an axisymmetric cylinder, the expressions for the non-zero components reduce to

$$\begin{aligned} F_{\eta_4} = {} & -\frac{\pi\rho R^2h^2}{2}\left(g\eta_4 + \ddot{\eta}_2\right) - J_{01}^1\ddot{\eta}_4 \\ & - \sum_{j=1}^{I_r}\left[\frac{g\pi\rho R^3}{l_{1,j}^2}\beta_{1,j,1} + \frac{2\pi\rho R^4\tanh\left(\frac{h}{2R}l_{1,j}\right)}{l_{1,j}^3}\ddot{\beta}_{1,j,1}\right] \end{aligned} \tag{26}$$

$$\begin{aligned} F_{\eta_5} = {} & -\frac{\pi\rho R^2h^2}{2}\left(g\eta_5 + \ddot{\eta}_1\right) - J_{02}^1\ddot{\eta}_5 \\ & + \sum_{j=1}^{I_r}\left[\frac{g\pi\rho R^3}{l_{1,j}^2}\beta_{1,j,2} + \frac{2\pi\rho R^4\tanh\left(\frac{h}{2R}l_{1,j}\right)}{l_{1,j}^3}\ddot{\beta}_{1,j,2}\right] \end{aligned} \tag{27}$$

$$J_{01}^1 = J_{02}^1 = \pi\rho R^2\left[\frac{1}{3}h^3 - \frac{3}{4}hR^2 + 16R^3\sum_{j=1}^{I_r}\frac{\tanh\left(\frac{h}{2R}l_{1,j}\right)}{l_{1,j}^3\left(l_{1,j}^2 - 1\right)}\right] \tag{28}$$

where the non-zero components (J_{01}^1 and J_{02}^1) of the so-called Joukowsky inertial tensor are given as in Tan et al. (2019) after correcting the typo

in the original expression by Faltinsen and Timokha (2009). Note also that Eqs. 23–27 are given in the cage-fixed coordinate system with the origin in the centre of the equilibrium free surface of the liquid.

2.5. Scaled physical experiment

Physical experiments with a scaled model of cylindrical closed rigid cage were performed in the Ocean Basin of SINTEF Ocean. To ensure similarity of relevant physical parameters (e.g. velocities, forces and moments) between full scale and model scale, Froude scaling was applied with a chosen scale factor of 1:27. The basin is 80 m long, 50 m wide, and equipped with an adjustable floor. The depth was set to 5 m, equivalent to 135 m in full scale, thereby assuming deep water condition for the selected waves.

The main dimensions and a sketch of the model are given in Fig. 1, where the ratio of cage depth to cage diameter is equal to 0.5 ($h/D = 0.5$). The model was made of polycarbonate resin (Lexan), reinforced with aluminium plates (along the side wall) and steel tubes (exterior to the bottom) to reduce the flexibility of the cage. The cage tank was filled with water up to the design mean water line. The freeboard was 0.35 m from the mean water line to the top rim of the model. To ensure sufficient stability and buoyancy, a torus shaped floating collar (made of plastic electrical tube and reinforced with two aluminium rings) was attached to the cage model. The model was located in the centre of the basin, with incoming waves generated in line with the global x-axis as shown in Fig. 1. The mooring configuration consisted of four equally spaced mooring lines which were attached to the floating collar, centred in the design mean water line of the cage. The other end of each mooring line was attached far away to a horizontal free-hanging coil spring. The stiffness of each coil spring was 60 N/m and a pretension of 45 N was applied to all mooring lines, yielding an equivalent horizontal stiffness (in x and in y directions as shown in Fig. 1) of 170 N/m for the system. The pretension in the mooring lines also provided an additional pitch restoring coefficient of 67.5 Nm/rad (approximated as the mooring line pretension multiplied by cage diameter).

The model was tested in regular waves with the wave periods in the range between 0.63 s and 2.5 s (some of the test runs were not performed due to time constrains), corresponding to the relative wavelengths (i.e. the ratio of wavelength to cage diameter λ/D) in the range from 0.41 to 6.5. Irregular wave tests were performed using a typical JONSWAP spectrum, with four different combinations of peak period (T_p) and significant wave height (H_s). Prior to the testing, the wave field was calibrated without the presence of the model and a wave probe (Wave2) was used to measure wave elevations in the centre of the basin (where the model would be located). All tests were performed with 100% filling ratio, such that the water level inside the model was same as the external mean free surface.

In the testing, motions of the cage were measured using an optical positioning system where the positions of the reflective markers (Pos1-8) mounted along the cage side wall (32–328° with respect to the positive x-axis) were tracked from camera images. Three accelerometers (Acc1-3) were also mounted on the model for a benchmark check of the measured motions from the optical positioning markers. Sloshing of the contained water inside the cage and the wave elevation outside were measured by a set of wave probes (RW1-8: internal wave probe; RW9-16: external wave probe) distributed along the circumferential direction (22–337° with respect to the positive x-axis) of the cage and with a radial distance of $D/40$ from the side wall. Two more wave probes (Wave1 and Wave3) were installed 5 m away from the model to measure the front and side waves. Tensions in the mooring lines were measured by the uni-axial load cells (L1-4) installed between the cage and each mooring line.

A thorough description of the model and instrumentation setup can be found in Shen et al. (2021), as well as the measurement accuracy (e.g. the specified measurement errors of the optical positioning marker and the wave probe were below 0.2 mm and 1.0 mm, respectively) and processing of the experimental data. These are not further discussed in the present paper, while the analysed data by Shen et al. (2021) are used for comparisons with the numerical simulation results.

2.6. Simulation experiments

The closed cage was modelled in WAMIT as a moored floating body in the water of infinite depth. The geometry of the physical model was discretized by an ensemble of flat quadrilateral panels (as shown in Fig. 2), where the geometrical representation of the floating collar was simplified to avoid numerical problems. Simplifications of the geometry representation were made such that the water-plane area and the displacement of the cage was conserved. An interior liquid tank (represented by the green panels in Fig. 2) was applied to model the coupling effects of the contained water on the rigid-body motions of the cage. The moorings were modelled as linear restoring forces with equivalent

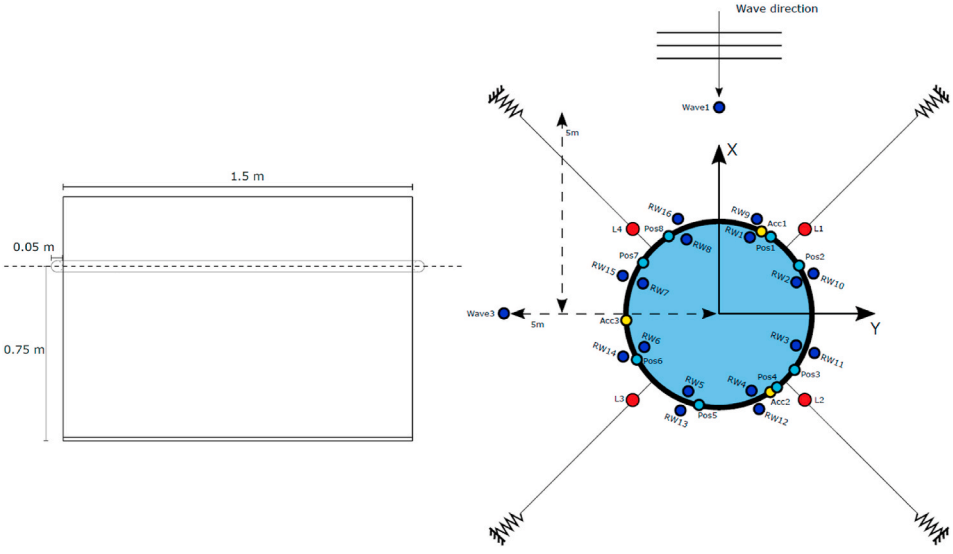

Fig. 1. Sketch of model geometry ($h/D = 0.5$) and instrumentation setup (Blue circles: internal and external wave probes; Cyan circles: optical positioning markers; Yellow circles: accelerometers; Red circles: force transducers). (For interpretation of the references to colour in this figure legend, the reader is referred to the Web version of this article.)

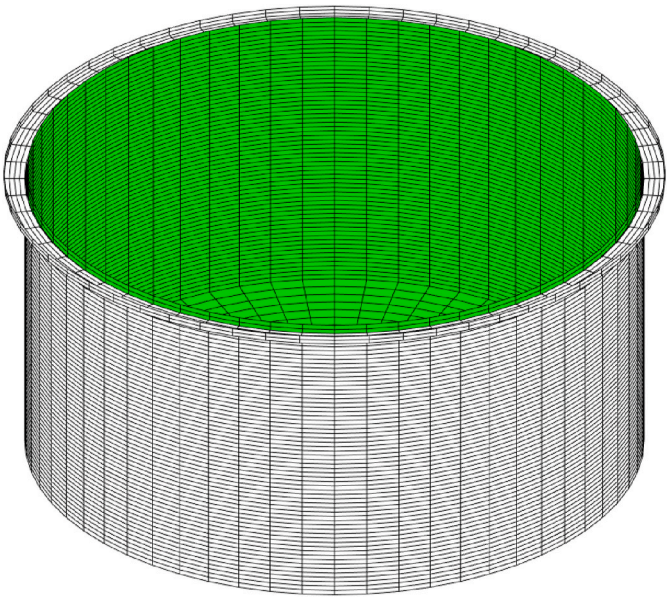

Fig. 2. Mesh of quadrilateral elements used in frequency-domain calculations with WAMIT.

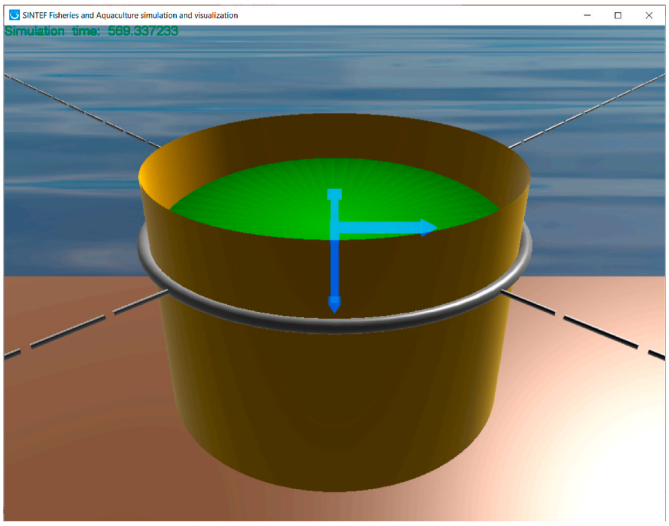

Fig. 3. Time-domain simulation setupfor the present model configuration $(h/D = 0.5)$ in FhSim.

spring constants from the physical experiment.

The time-domain simulation model in FhSim consists of the waves, the closed cage, the contained water and the mooring lines (as shown in Fig. 3), which were set up similarly to the physical experiment. The methods introduced in Sections 2.2 to 2.4 and the frequency-domain data obtained from the calculations with WAMIT were used to simulate the instantaneous responses of the cage and the mooring lines in both regular and irregular wave conditions.

In a previous experimental study (Kristiansen et al., 2018a), two model configurations were tested, i.e. a "wet" model where the closed cage was filled with water and a "dry" model where the contained water was replaced by fixed weights to resemble "frozen" water. These two cage models were made of same materials and had same dimensions as in the present experiment, except for the depth $(h/D = 0.25)$ which was 1/2 of the present model (as shown in Figs. 3 and 4). The same mooring lines and pretensions were used for the "wet" and "dry" models, which provided an equivalent horizontal stiffness of 180 N/m, close to the

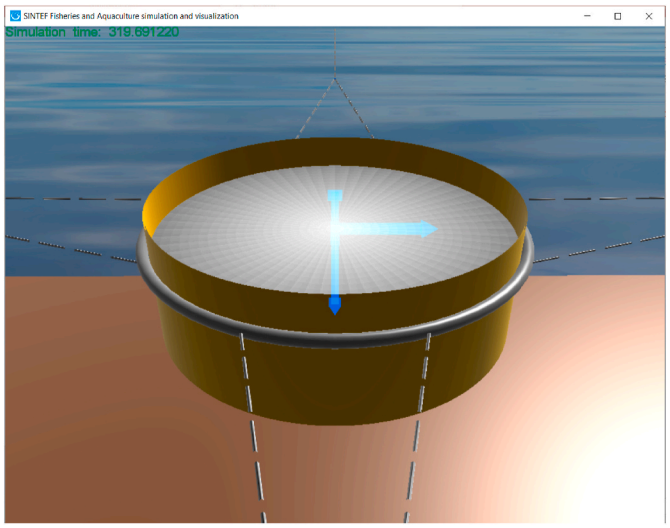

Fig. 4. Time-domain simulation setup for the "dry" and "wet" model configurations $(h/D = 0.25)$according to Kristiansen et al. (2018a).

present setup. Both of the "wet" and "dry" models were simulated in FhSim, as a supplementation to the present model for a better understanding of the influence of sloshing on the wave-induced responses of closed cages.

3. Results

The experimental data described in Section 2.5 and the corresponding numerical simulation results are presented in this section, with a focus on the global response of the cage. The results of decay tests are presented in the first place, followed by the results in regular and irregular waves. All values are presented in full scale, i.e. scaled up by Froude scaling with a chosen scale factor of 1:27.

3.1. Results of decay tests

Free decay tests were performed to identify the natural periods of cage motions and the corresponding damping levels. The testes were started by giving the model an initial perturbation from equilibrium in the considered mode of motion, trying to minimize the coupling with other modes. The nonlinear viscous damping was considered in the time-domain simulations (FhSim) by using a drag coefficient of 0.6, which was evaluated based on the model test data of a similar cylindrical

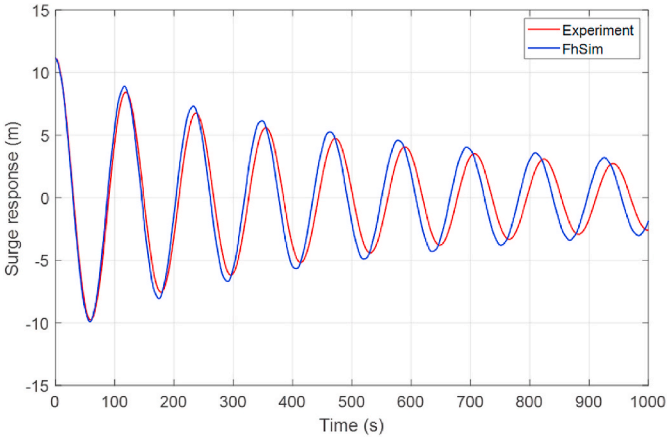

Fig. 5. Time series of the measured and simulated surge decay responses for the present model configuration $(h/D = 0.5)$.

structure in current (Fokk, 2010).

As shown in Fig. 5, the simulated surge decay responses are in good agreement with the experimental results. The surge natural periods obtained from the experiment and the time-domain simulation are 116.4 s and 115.6 s, respectively. The corresponding damping ratios are 0.026 and 0.024. The heave natural period obtained from the time-domain simulation (Fig. 6) is 10.6 s and the corresponding damping ratio is 0.055, while there is no experimental data on the heave decay response. The pitch natural period obtained from the experiment (Fig. 7) is 14.4 s, the simulation result is about 9% smaller, i.e. 13.1 s. The corresponding damping ratios are 0.095 and 0.066, respectively. The differences between the numerical and model test results (especially for the pitch response) are mainly attributed to the simplified body geometry in the numerical model, where the hydrostatic restoring coefficients were assumed to be constant (corresponding to the mean water-plane) while it was observed in the model tests that the floating collar could easily go in and out of water due to small draft, causing time-dependent restoring force or moment (Shen et al., 2021).

The decay tests do not provide information about the coupled natural periods between cage motions (surge and pith) and sloshing, as it takes a long transient phase with given forcing frequency to develop steady-state internal waves. The natural sloshing periods, $T_{m,i}$, associated with the first four azimuthal ($m = 0, 1, 2, 3$) and two radial ($i = 1, 2$) modes defined by the multi-modal method (Eq. (10)) are presented in Table 1, as well as the calculated natural periods of cage motions.

3.2. Results in regular waves

In the physical experiments, the incident waves were documented by wave calibration tests for all wave conditions with no model present in the basin. The generated incident waves at the model location were found to be in agreement with the wave parameters input to the wavemaker for the major part of the test wave conditions. Typical time series obtained from the regular wave tests and the corresponding time-domain simulations are presented in Figs. 8–10. For each test/simulation, a time window was chosen from where steady-state values of incident wave height and corresponding rigid-body motion amplitudes were extracted. The calculated response amplitude operators (RAO's) for surge, heave and pitch are presented in Figs. 11–13, respectively, where the steady-state motion amplitudes are normalized by the measured/simulated incident wave amplitudes.

The obtained time series from the simulation and the calculated surge, heave, and pitch RAO's are in good agreement with the experimental results for wave periods shorter than 7 s. The increased deviations for longer wave periods are attributed to the difference in the pitch natural period predicted by FhSim (13.1 s) relative to that

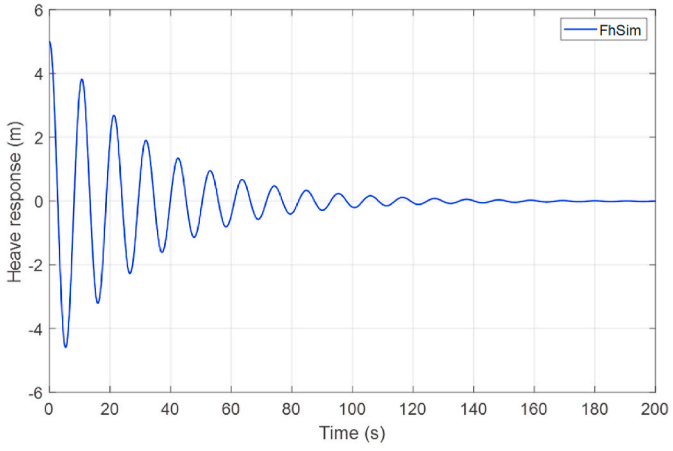

Fig. 6. Time series of the simulated heave decay responses for the present model configuration ($h/D = 0.5$).

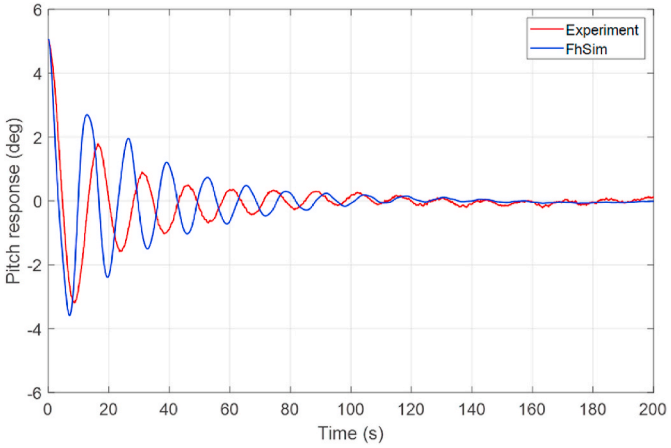

Fig. 7. Time series of the measured and simulated pitch decay responses for the present model configuration ($h/D = 0.5$).

Table 1
Calculated natural periods of cage motions and sloshing for the present model configuration ($h/D = 0.5$).

Cage motions		Sloshing	
Surge	115.6 s	$T_{0,1}$	4.61 s
Heave	10.6 s	$T_{1,1}$	6.82 s
Pitch	13.1 s	$T_{2,1}$	5.18 s
		$T_{3,1}$	4.41 s
		$T_{0,2}$	3.41 s
		$T_{1,2}$	3.91 s
		$T_{2,2}$	3.49 s
		$T_{3,2}$	3.19 s

obtained from the experiment (14.9 s). The RAO's obtained from the frequency-domain simulation (WAMIT) are also presented in Figs. 11–13, and they are in good agreement with the time-domain simulation results for the major part of wave periods. In addition, the surge, heave and pitch natural periods predicted by WAMIT coincide with those predicted by FhSim. Due to coupling effects, large surge motions are predicted around the pitch resonance period. By applying an additional pitch damping ratio ($\zeta_p + 0.05$, added damping equal to 5% of critical damping) in the time-domain simulation, the obtained surge RAO's around the pitch natural period are more comparable with the experimental results. Fig. 14 shows the time series of the simulated pitch responses around the resonance period and comparison with the experimental results. The response amplitudes obtained from the experiment and simulation tend to be in the same range. However, the measured responses seem to be unsteady during the limited testing time and the dominant period is not associated with the wave period. Therefore, the pitch RAO is not calculated for this test wave condition (Period: $T = 12.99$ s; Steepness: $H/\lambda = 1/60$). The cage model used in the physical experiment was not fully rigid. This could have influenced the comparisons between the experimental and numerical results, as well as the nonlinear hydrodynamic effects that have not been considered in the numerical models. For example, submergence of local sections of the floating collar due to the waves will cause a time-dependent pitch restoring moment. This effect is not included in the present numerical model where a linear restoring moment corresponding to the mean water-plane area is used.

In the experiments, a nonlinear phenomenon of sub-harmonic response (in pitch) is observed for the wave period $T = 12.99$ s, as shown in Fig. 14. The same behaviour is not observed in the simulations. The pitch response in the first part of the measured time-series follows the wave period, while about 550 s after start-up, a process with the doubling of the response period is seen to emerge. Following the

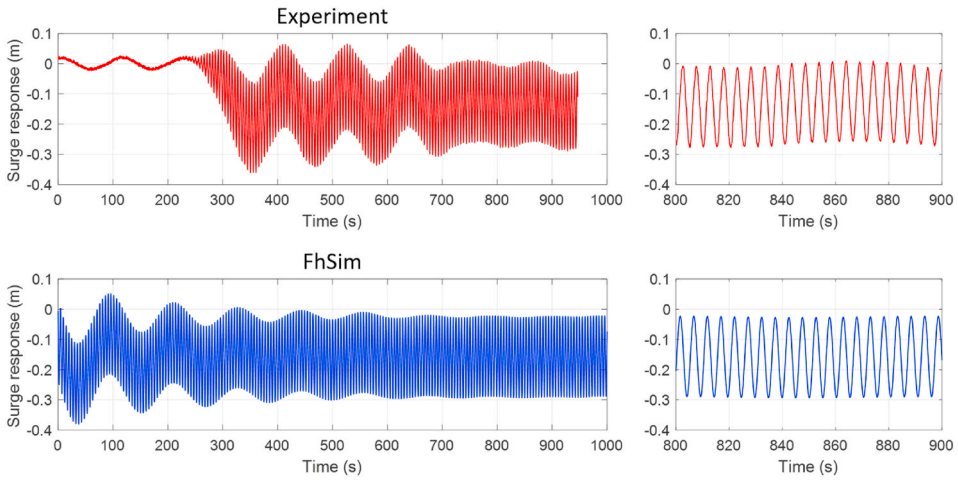

Fig. 8. Time series of the measured and simulated surge responses in regular wave (Period: $T = 5.11$ s; Steepness: $H/\lambda = 1/45$) for the present model configuration ($h/D = 0.5$).

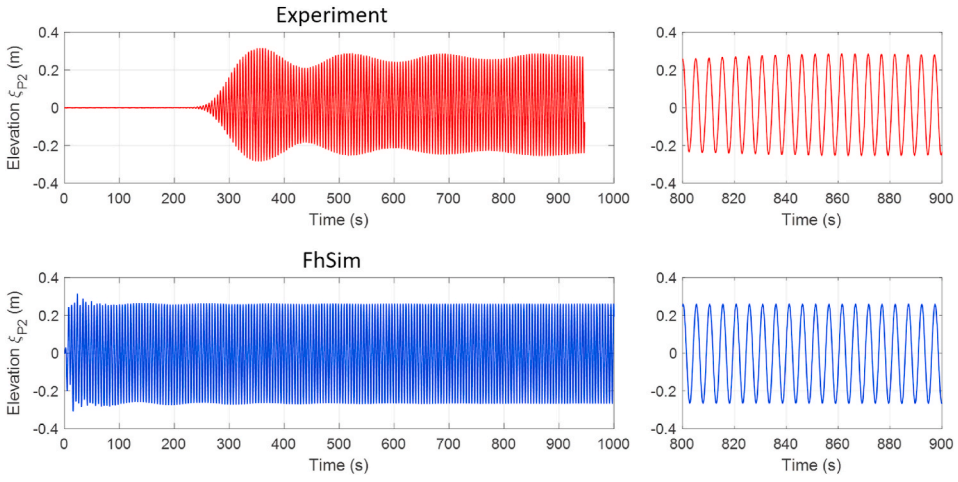

Fig. 9. Time series of the measured and simulated internal water surface elevations (at the measuring point RW2, i.e. 67° with respect to the positive x-axis and $D/40$ from the cage side wall, as shown in Fig. 1) in regular wave (Period: $T = 5.11$ s; Steepness: $H/\lambda = 1/45$) for the present model configuration ($h/D = 0.5$).

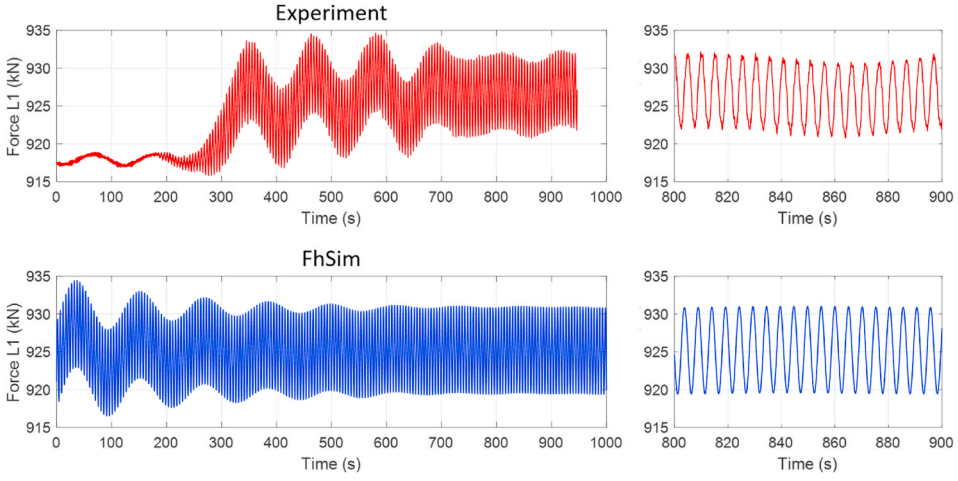

Fig. 10. Time series of the measured and simulated mooring forces (mooring line L1) in regular wave (Period: $T = 5.11$ s; Steepness: $H/\lambda = 1/45$) for the present model configuration ($h/D = 0.5$).

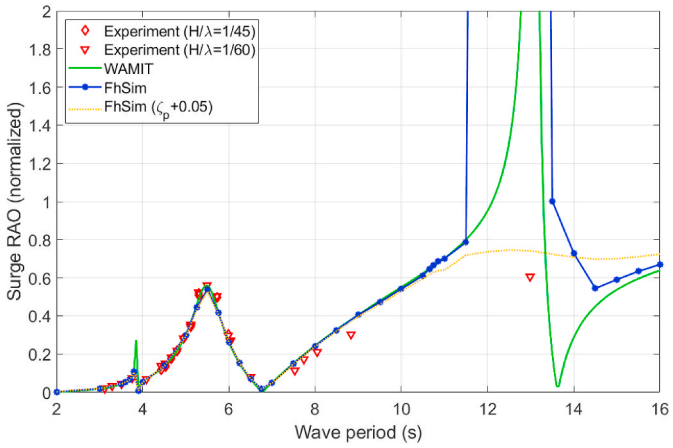

Fig. 11. Comparison of the measured and simulated surge RAO's (η_1/A) in regular waves for the present model configuration ($h/D = 0.5$).

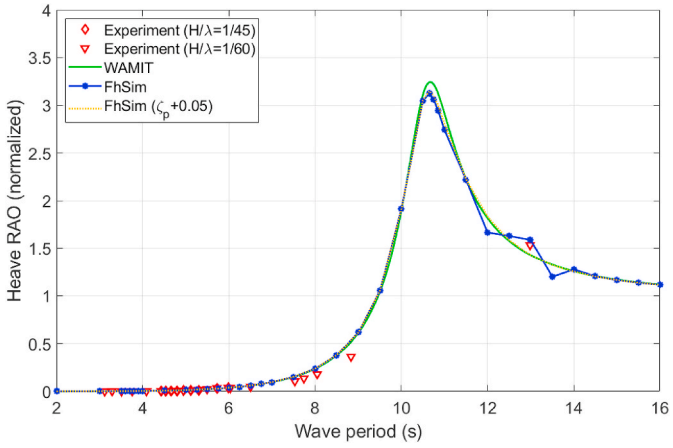

Fig. 12. Comparison of the measured and simulated heave RAO's (η_3/A) in regular waves for the present model configuration ($h/D = 0.5$).

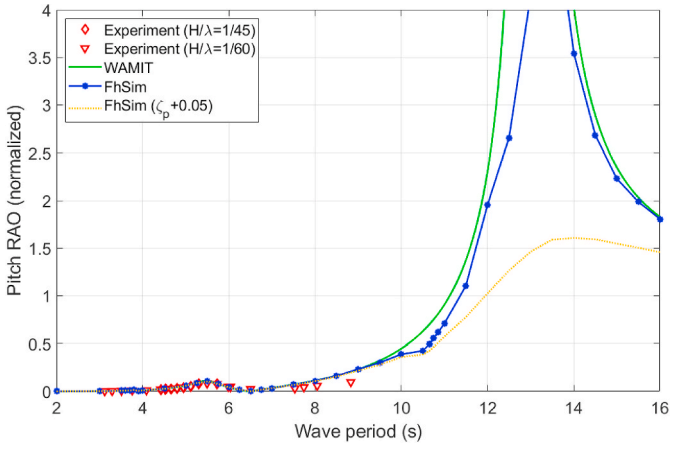

Fig. 13. Comparison of the measured and simulated pitch RAO's (η_5/kA) in regular waves for the present model configuration ($h/D = 0.5$).

doubling of the response period is a significant increase of the response amplitude. A typical example of sub-harmonic response in marine hydrodynamics is so-called parametric rolling (of ships), where a time-dependent "quasi-static" restoring moment in roll due to the waves causing a "parametric excitation". This effect is not further discussed in the present paper, due to the limited experimental data (only for the wave period $T = 12.99$ s).

3.3. Results in irregular waves

The long-crested irregular wave tests and simulations were performed using a standard JONSWAP spectrum (peakedness factor: 3.3), with four different combinations of the input peak periods and significant wave heights: $T_p = [5.0\ \text{s}, 6.0\ \text{s}, 7.8\ \text{s}, 10.0\ \text{s}]$; $H_s = [1.5\ \text{m}, 2.0\ \text{m}, 3.0\ \text{m}, 3.0\ \text{m}]$. Examples of the time series obtained from the experiments and the time-domain simulations in irregular waves are presented in Figs. 15–18. The power spectra of the corresponding surge responses are shown in Fig. 19.

The obtained time series from the simulation are, in general, comparable with the experimental results. The measured pitch motions (Fig. 16) and internal water surface elevations (Fig. 17) show a higher degree of nonlinearities, which can be attributed to the time-dependent pitch restoring coefficient and the ovalizing deformation modes of the cage, according to Shen et al. (2021). These effects are not considered in the present numerical models and remain to be further investigated.

As shown in Fig. 19, the dominant low-frequency responses in irregular waves correspond to the resonance oscillations excited around the surge natural frequency (≈ 0.009 Hz) of the moored system, due to the slow-drift forces. The amplitudes of the slow-drift motions of the cage are found to be considerably larger than the first-order responses (associated with the incoming wave frequencies) in the four tested/simulated irregular wave conditions.

4. Discussions

4.1. The influence of sloshing on cage responses

Comparisons of obtained RAO's from the experiments (Kristiansen et al., 2018a) and the corresponding numerical simulations (WAMIT and FhSim) with the "dry" and "wet" model configurations in regular waves show large impact of sloshing on the surge and pitch motions of the cage (Figs. 20 and 22) while no visible impact on the heave motion (Fig. 21). The heave RAO's obtained from the experiments with the "dry" and "wet" model configurations were almost identical. This is consistent with linear potential flow theory that there is no influence of sloshing on the heave motion (Newman, 2005; Faltinsen and Timokha, 2009).

As shown in Fig. 20, the surge response amplitudes are amplified by about 200% for wave periods around the natural period ($T_{2,1} = 5.40$ s) of sloshing corresponding to the symmetric mode shape $\sigma_{2,1}$ (see the definition in Eq. (10)). However, according to linear potential flow theory, symmetric sloshing modes does not yield any surge force. The local maximum of the surge RAO around $T_{2,1} = 5.40$ s for the "wet" model is attributed to the frequency-dependent added mass of the contained water being negative for the actual frequency and hence cancelling out parts of the inertia force (reducing the effective mass of the structure). By applying an additional modal damping ratio ($\zeta_m + 0.05$) in the time-domain simulation (FhSim) with the "wet" model configuration, i.e. when sloshing was damped, lower surge RAO's were obtained around this frequency. This result further indicates the influence of sloshing on the surge motion of the cage.

In the experiments with the "wet" model configuration, a nonlinear effect of wave steepness on the surge response was observed around $T_{2,1}$, which could not be captured by the linear (WAMIT) and weakly nonlinear (FhSim) sloshing models. It is noted that the nonlinearity appears as an excitation, causing the response to increase with increasing wave steepness. In the experiments, the cage model was also

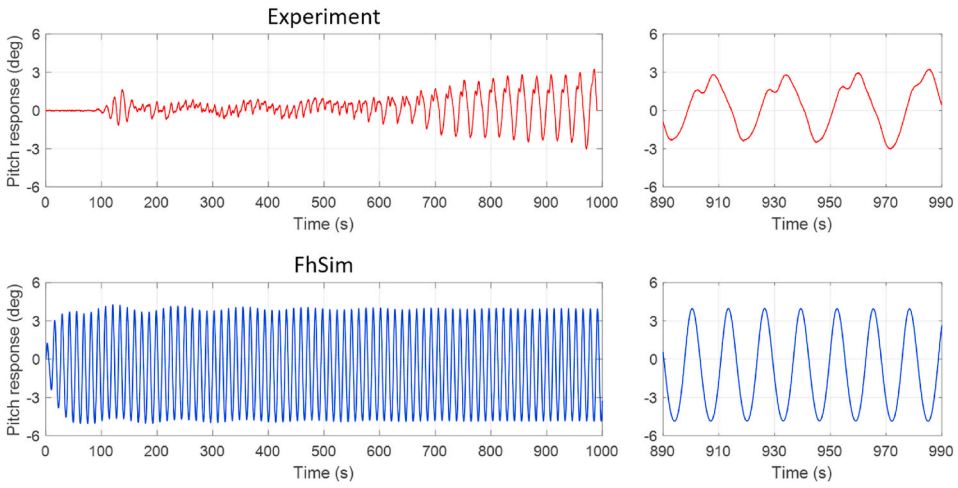

Fig. 14. Time series of the measured and simulated pitch responses in regular wave (Period: $T = 12.99$ s; Steepness: $H/\lambda = 1/60$) for the present model configuration ($h/D = 0.5$).

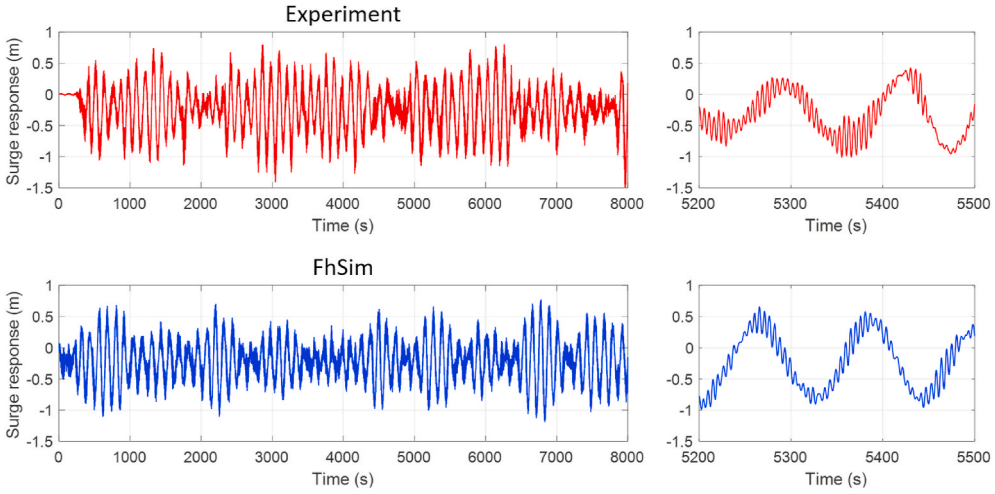

Fig. 15. Time series of the measured and simulated surge responses in irregular wave (Peak period: $T_p = 5.0$ s; Significant wave height: $H_s = 1.5$ m) for the present model configuration ($h/D = 0.5$).

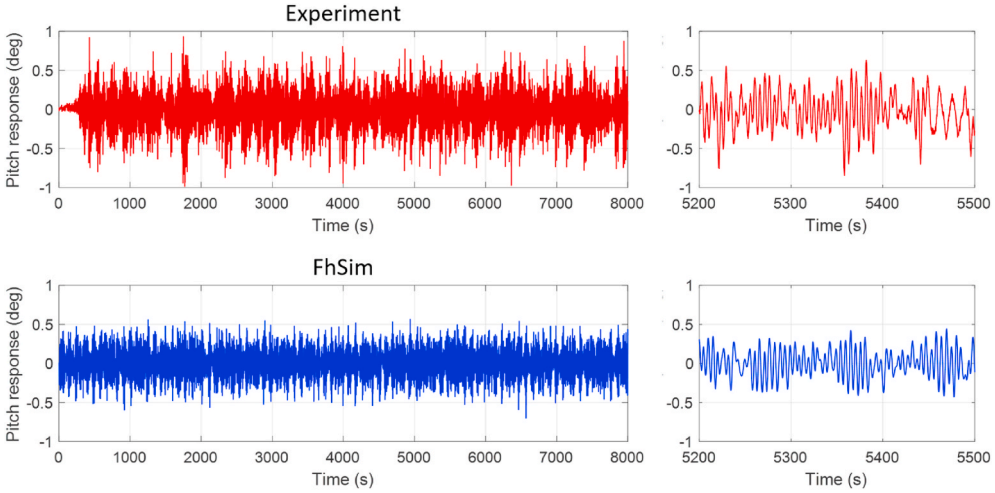

Fig. 16. Time series of the measured and simulated pitch responses in irregular wave (Peak period: $T_p = 5.0$ s; Significant wave height: $H_s = 1.5$ m) for the present model configuration ($h/D = 0.5$).

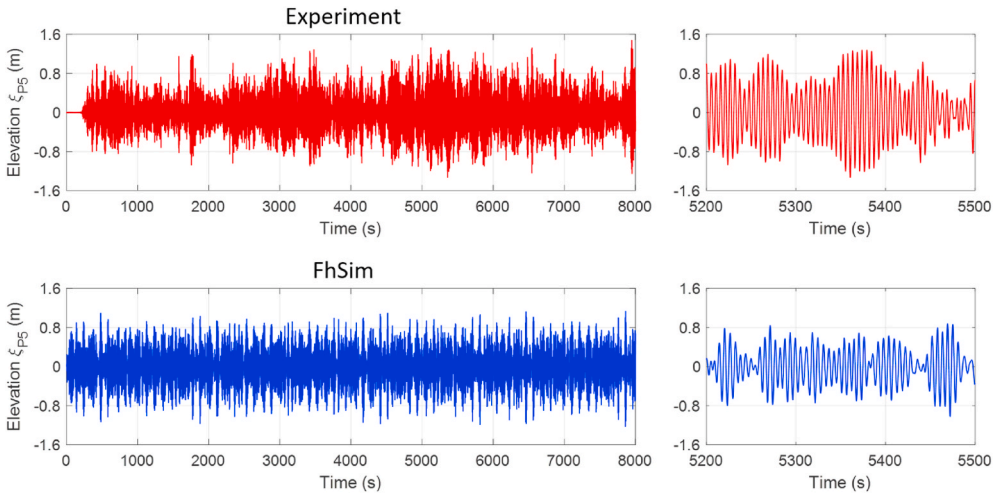

Fig. 17. Time series of the measured and simulated internal water surface elevations (at the measuring point RW5, i.e. 202° with respect to the positive x-axis and $D/40$ from the cage side wall, as shown in Fig. 1) in irregular wave (Peak period: $T_p = 5.0$ s; Significant wave height: $H_s = 1.5$ m) for the present model configuration ($h/D = 0.5$).

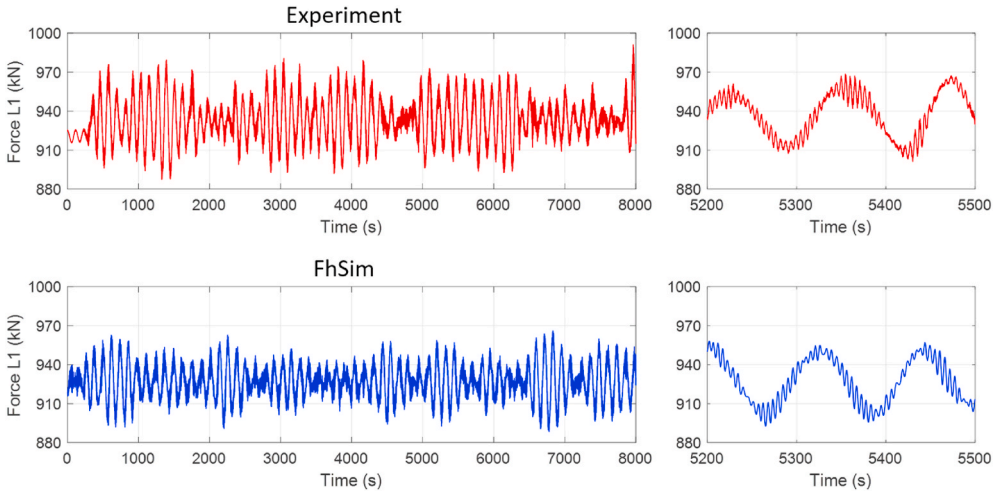

Fig. 18. Time series of the measured and simulated mooring forces (mooring line L1) in irregular wave (Peak period: $T_p = 5.0$ s; Significant wave height: $H_s = 1.5$ m) for the present model configuration ($h/D = 0.5$).

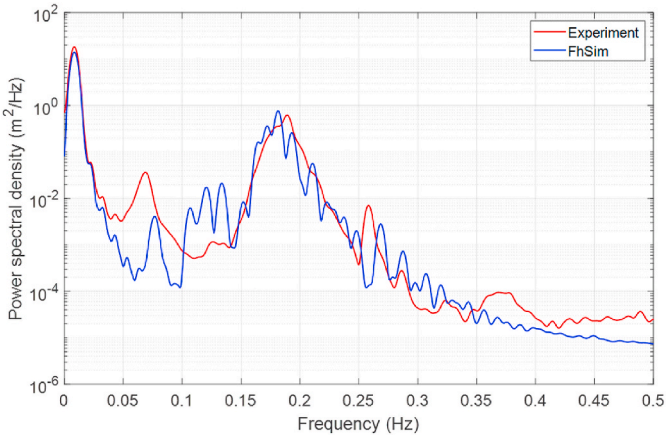

Fig. 19. Power spectra of the measured and simulated surge responses in irregular wave (Peak period: $T_p = 5.0$ s; Significant wave height: $H_s = 1.5$ m) for the present model configuration ($h/D = 0.5$).

observed to perform elastic deformations characterized by ovalizing of the water-plane cross-section for this case.

As shown in Fig. 22, the pitch motion amplitudes of the "wet" model are largely reduced compared to those of the "dry" model around the pitch resonance period. This is because the presence of internal free surface has a destabilizing effect that increases the pitch natural period of the cage. For both the "dry" and "wet" model configurations, deviations were observed between the measured and simulated pitch motions. This is also attributed to the difference in the pitch natural period predicted by WAMIT and FhSim relative to that obtained from the experiment. The results obtained from the time-domain simulations (FhSim) are, in general, more comparable with the experimental results when an additional modal damping ratio ($\zeta_m + 0.05$) was applied for longer wave periods, especially around the pitch natural period of the cage.

4.2. Mean-drift forces in regular waves

Comparisons of the measured and simulated time series of mooring line tensions in regular waves show that the mean-drift forces are considerable and influenced by sloshing (Fig. 23). In the experiments

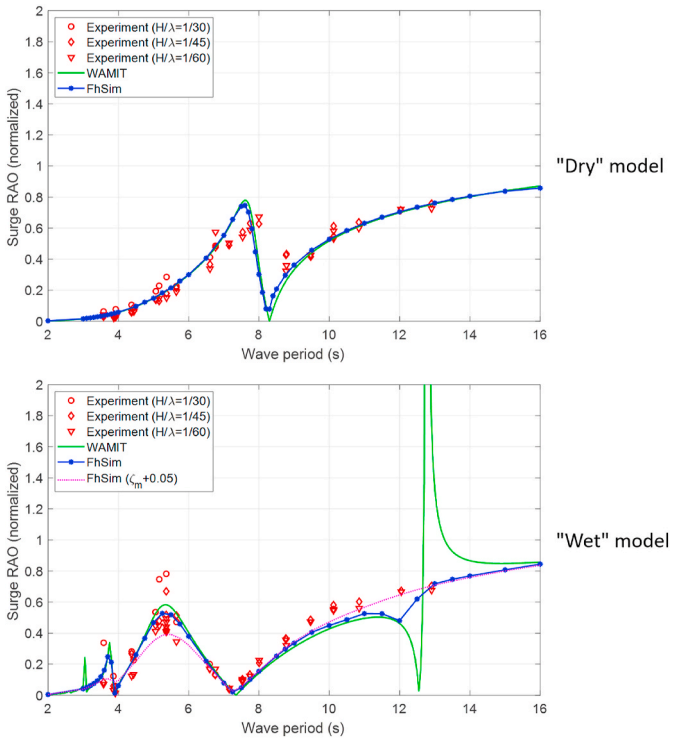

Fig. 20. Comparison of the measured (experimental data from Kristiansen et al. (2018a)) and simulated (WAMIT and FhSim) surge RAO's (η_1/A) for the "dry" and "wet" model configurations ($h/D = 0.25$).

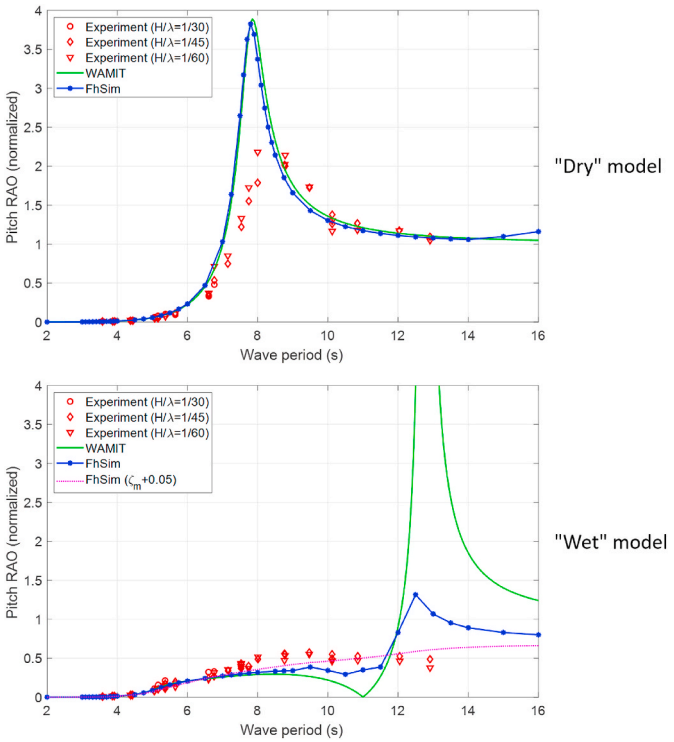

Fig. 22. Comparison of the measured (experimental data from Kristiansen et al. (2018a)) and simulated (WAMIT and FhSim) pitch RAO's (η_5/kA) for the "dry" and "wet" model configurations ($h/D = 0.25$).

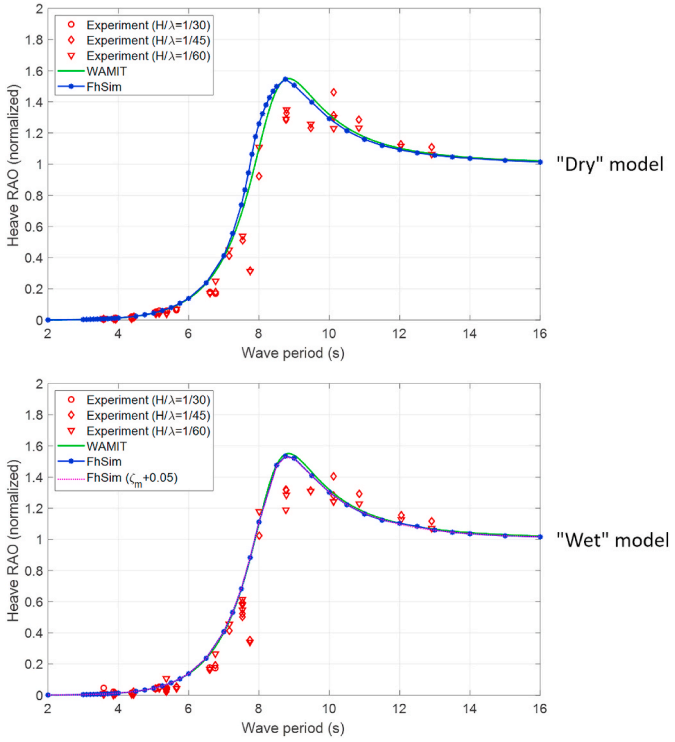

Fig. 21. Comparison of the measured (experimental data from Kristiansen et al. (2018a)) and simulated (WAMIT and FhSim) heave RAO's (η_3/A) for the "dry" and "wet" model configurations ($h/D = 0.25$).

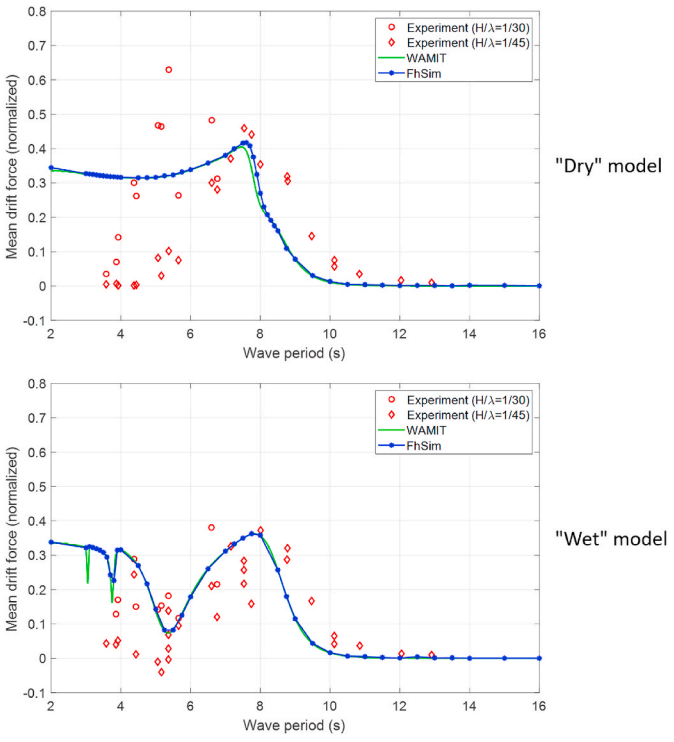

Fig. 23. Comparison of the measured (experimental data from Kristiansen et al. (2018a)) and simulated (WAMIT and FhSim) mean drift forces ($\overline{F}_1/\rho g A^2 D$) for the "dry" and "wet" model configurations ($h/D = 0.25$).

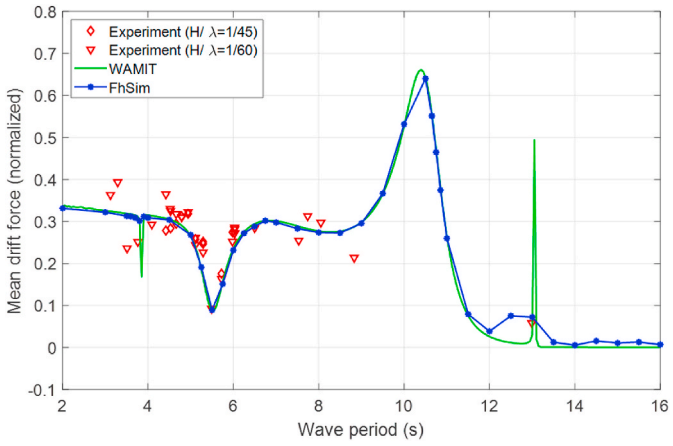

Fig. 24. Comparison of the measured and simulated mean drift forces ($\overline{F}_1/\rho g A^2 D$) for the present model configuration ($h/D = 0.5$).

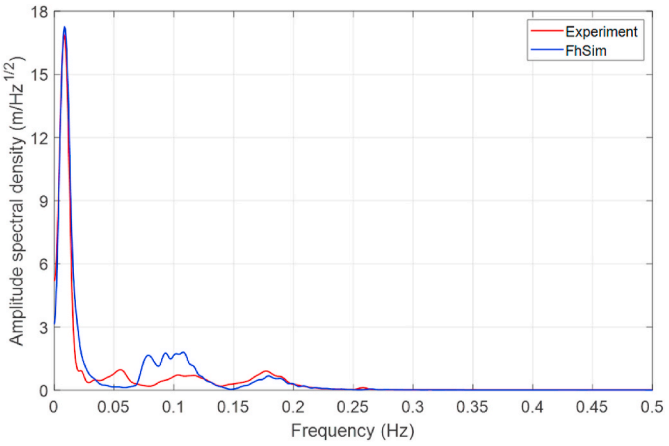

Fig. 26. Amplitude spectra of the measured and simulated surge responses in irregular wave (Peak period: $T_p = 7.8$ s; Significant wave height: $H_s = 3.0$ m) for the present model configuration ($h/D = 0.5$).

with the "dry" and "wet" model configurations (Kristiansen et al., 2018a), wave reflections from the side walls of the towing tank were also found to have large influence on the mean-drift forces and result in large scatter of the measurement results. These effects were negligible in the present experiments, as the ocean basin is considerably wide and equipped with absorption beaches along both the short and long basin sides which reduce wave reflections to a minimum. The present experimental results (Fig. 24) show a clear influence of sloshing on the mean-drift forces when the surge response is amplified due to sloshing (for wave periods around 5.5 s, as shown in Fig. 11), which is consistent with the numerical results. Other effects that could have influenced the measured mean-drift forces were the precision of the load cells when measuring small quantities, the nonlinear hydrodynamic effects due to the in and out of water motion of the floating collar in waves, and the elastic deformation of the cage.

4.3. *Slow-drift forces in irregular waves*

The surge motion of the cage and the resulting mooring line forces were found to be dominated by the slow-drift effects in the four tested/simulated irregular wave conditions. Fig. 25 shows the time series of the measured and simulated surge responses in the irregular wave ($T_p = 7.8$ s; $H_s = 3.0$ m), where the dominant frequency (≈ 0.009 Hz) corresponds to the surge natural frequency of the cage (Fig. 26). Fig. 27 shows the time series of the simulated surge responses in a comparative regular wave condition ($T = 7.8$ s; $H = 3.0$ m), where the dominant frequency (≈ 0.128 Hz) is associated with the incoming wave frequency (Fig. 28). The amplitudes of the dominant slow-drift motions in the irregular wave are about 500% larger than the dominant first-order motions in the regular wave. The corresponding mooring forces are also considerably larger in the irregular wave (Fig. 29) as compared with the forces in the regular wave (Fig. 30). Fig. 31 shows the filtered time series of the

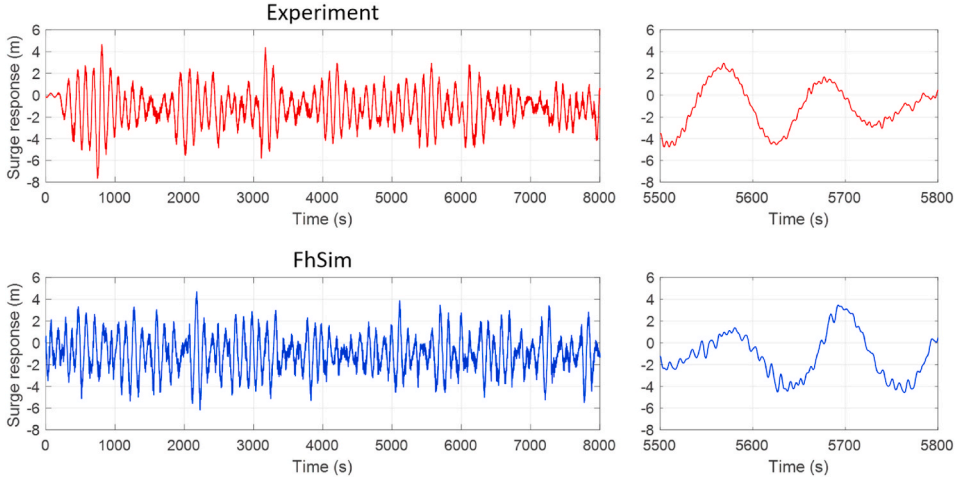

Fig. 25. Time series of the measured and simulated surge responses in irregular wave (Peak period: $T_p = 7.8$ s; Significant wave height: $H_s = 3.0$ m) for the present model configuration ($h/D = 0.5$).

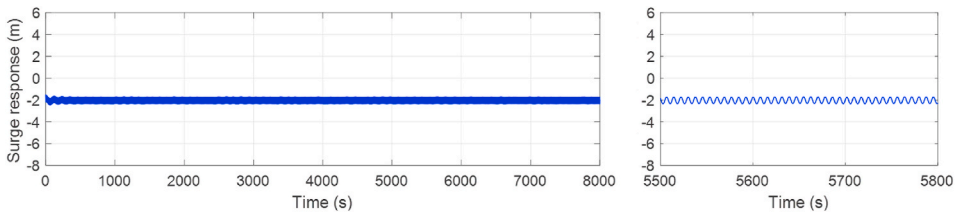

Fig. 27. Time series of the simulated surge responses in regular wave (Period: $T = 7.8$ s; Wave height: $H = 3.0$ m) for the present model configuration ($h/D = 0.5$).

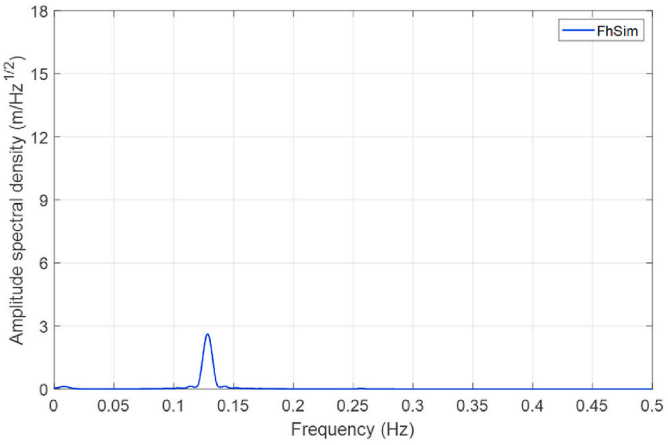

Fig. 28. Amplitude spectra of the simulated surge responses in regular wave (Period: $T = 7.8$ s; Wave height: $H = 3.0$ m) for the present model configuration ($h/D = 0.5$).

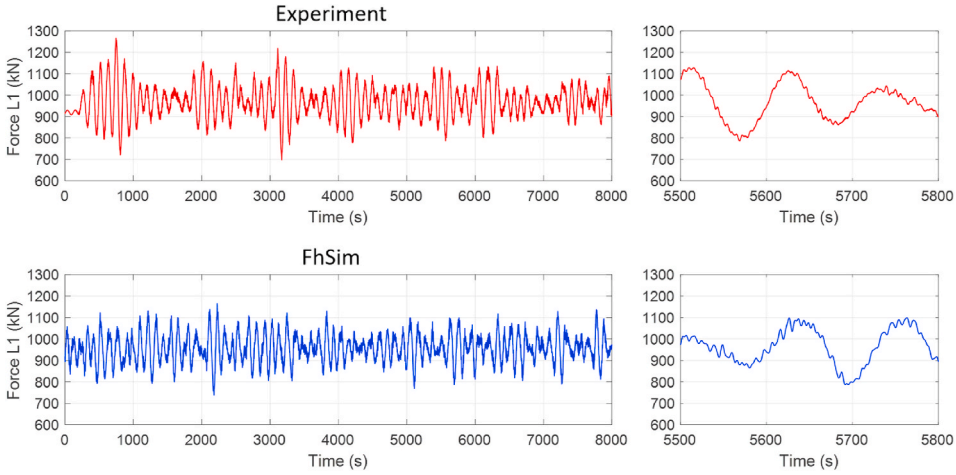

Fig. 29. Time series of the measured and simulated mooring forces (mooring line L1) in irregular wave (Peak period: $T_p = 7.8$ s; Significant wave height: $H_s = 3.0$ m) for the present model configuration ($h/D = 0.5$).

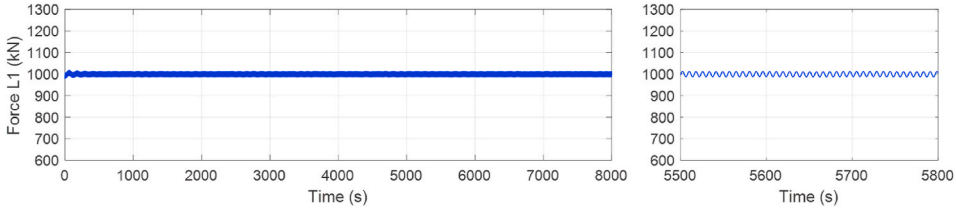

Fig. 30. Time series of the simulated mooring forces (mooring line L1) in regular wave (Period: $T = 7.8$ s; Wave height: $H = 3.0$ m) for the present model configuration ($h/D = 0.5$).

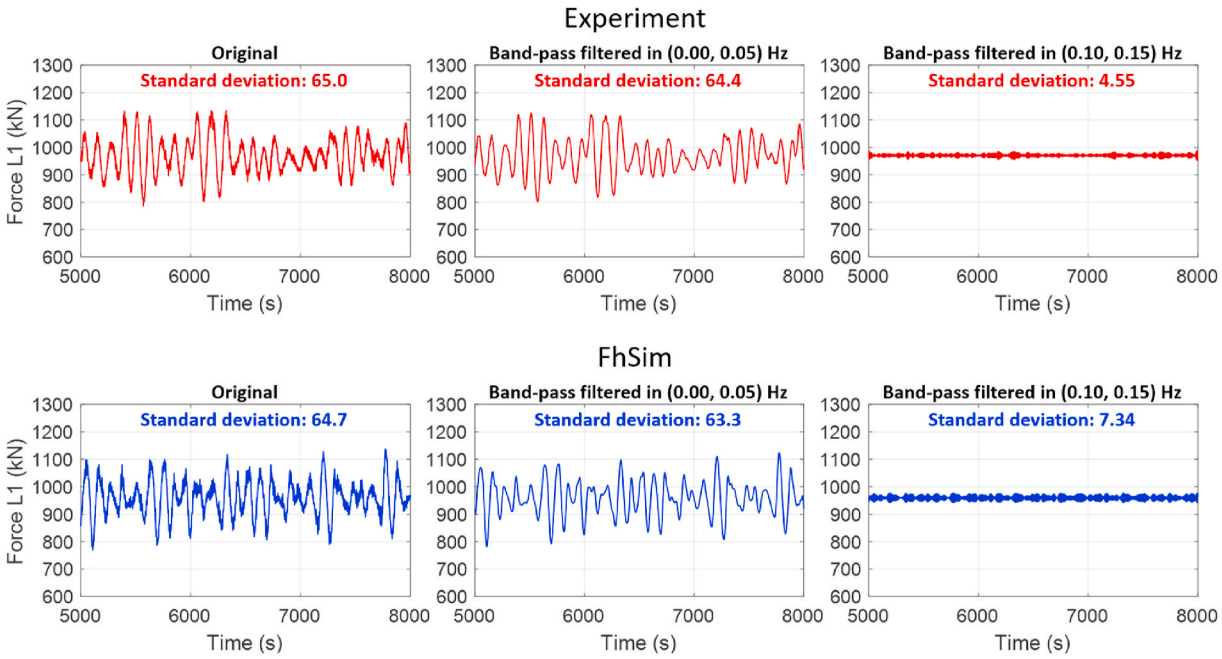

Fig. 31. Filtered time series of the measured and simulated mooring forces (mooring line L1) in irregular wave (Peak period: $T_p = 7.8$ s; Significant wave height: $H_s = 3.0$ m) for the present model configuration ($h/D = 0.5$).

mooring forces (using band-pass filtering) in the irregular wave, where the calculated standard deviations of the low-frequency components (0–0.05 Hz) are found to be much larger than the high-frequency components (0.1–0.15 Hz), and very close to the standard deviations of the total forces (original). This further indicates that the slow-drift forces are of great importance in the mooring system analysis for a closed cage similar to the present configuration.

5. Conclusions

In the present paper, the seakeeping behaviour of a closed rigid fish cage in waves has been studied by numerical modelling both in the frequency domain (WAMIT) and in the time domain (FhSim). The numerical simulation results are compared with the measurement data obtained from scaled physical experiments. The main findings from the numerical and comparative studies are as follows:

- The linear frequency-domain simulations with WAMIT are able to evaluate the coupling effects of sloshing on the wave-induced rigid body motions of closed cage. The predicted surge, heave and pitch RAO's and mean-drift forces in regular waves are, in general, comparable with the experimental data.
- The results obtained from the time-domain simulations with FhSim are in good agreement with WAMIT for all the tested model configurations in regular waves. In addition, the time-domain simulations are able to evaluate the slow-drift motions of closed rigid cage in irregular waves and the local instantaneous forces from each mooring line. The corresponding results are, in general, comparable with the experimental data.
- The comparative analyses show that sloshing has large influence on the coupled surge and pitch motions of closed cage. Sloshing is also found to have significant effect on the mean-drift forces in regular waves, especially when the surge response is amplified due to sloshing.
- The amplitudes of the dominant slow-drift motions in the tested/simulated irregular waves are found to be considerably larger than the dominant first-order motions in regular waves, which indicates that the slowly-varying wave drift forces need to be considered in the design of the mooring system for a floating closed cage.
- The weakly nonlinear multi-modal method implemented in FhSim is able to model both the planar and swirling waves inside a cylindrical tank (Tsarau et al., 2021). However, analyses of the surface wave patterns and the corresponding sloshing modes are not the focus of the present study.
- The linear potential flow theory and the weakly nonlinear multi-modal method are not able to capture some nonlinear hydrodynamic effects that might have influenced the comparisons between the numerical and experimental results. The present time-domain simulation model needs to be extended for considering the relevant nonlinear hydrodynamic effects, as well as the elastic deformation of a closed cage, i.e. the hydroelastic effects.

CRediT authorship contribution statement

Biao Su: Conceptualization, Methodology, Software, Validation, Writing – original draft. **Andrei Tsarau:** Methodology, Software, Writing – original draft. **Per Christian Endresen:** Software, Writing – original draft. **David Kristiansen:** Conceptualization, Methodology, Writing – review & editing. **Pål Furset Lader:** Conceptualization, Writing – review & editing.

Declaration of competing interest

The authors declare that they have no known competing financial interests or personal relationships that could have appeared to influence the work reported in this paper.

Acknowledgements

This work was financed by the Research Council of Norway (grant no. 268402), the Norwegian Seafood Research Fund and the industry partners through the project "Safe operation of closed aquaculture cages in waves". The authors would like to acknowledge the contributions of Dr. Stefan Arenfeldt Vilsen, Dr. Yugao Shen and Dr. Reza Firoozkoohi for analysing and reporting the present experimental data.

References

Baumgarte, J., 1972. Stabilization of constraints and integrals of motion in dynamical systems. Comput. Methods Appl. Mech. Eng. 1, 1–16.

Cummins, W.E., 1962. The Impulse Response Function and Ship Motions. Technical Report. David Taylor Model Basin, Bethesda, USA.

Endresen, P.C., Birkevold, J., Føre, M., Fredheim, A., Kristiansen, D., Lader, P., 2014. Simulation and validation of a numerical model of a full aquaculture net-cage system. In: Proc. 33rd International Conference on Ocean, Offshore and Arctic Engineering, San Francisco (OMAE 2014).

Faltinsen, O.M., 1993. Sea Loads on Ships and Offshore Structures. Cambridge Ocean Technology Series. Cambridge University Press.

Faltinsen, O.M., Timokha, A.N., 2009. Sloshing. Cambridge University Press.

Fokk, T., 2010. Sevan LUVA FSU - Model Tests Main Report. Technical Report. MARINTEK, Trondheim, Norway.

Fossen, T.I., 2005. A nonlinear unified state-space model for ship maneuvering and control in a seaway. International Journal of Bifurcation and Chaos 15 (9), 2717–2746.

Gustavsen, B., Semlyen, A., 1999. Rational approximation of frequency domain responses by vector fitting. IEEE Trans. Power Deliv. 14 (3), 1052–1061.

Gustavsen, B., 2006. Improving the pole relocating properties of vector fitting. IEEE Trans. Power Deliv. 21 (3), 1587–1592.

Johansen, V., 2007. Modelling of Flexible Slender Systems for Real-Time Simulations and Control Applications. PhD Thesis. Norwegian University of Science and Technology, Norway.

Kristiansen, D., Lader, P., Endresen, P.C., Aksnes, V., 2018a. Numerical and experimental study on the seakeeping behavior of floating closed rigid fish cages. In: Proc. 37th International Conference on Ocean. Offshore and Arctic Engineering, Madrid, Spain.

Kristiansen, D., Su, B., Volent, Z., 2018b. Numerical and experimental study on the drainage and collapse of a floating flexible bag structure. J. Fluid Struct. 83, 429–447.

Kristiansen, E., Egeland, O., 2003. Frequency-dependent added mass in models for controller design for wave motion damping. In: Proc. IFAC Conference on Maneuvering and Control of Marine Systems, Girona (MCMC'03).

Kristiansen, E., 2005. State Space Representation of Hydrodynamic Memory Effects. PhD Thesis. Norwegian University of Science and Technology, Norway.

Lader, P., Fredriksson, D.W., Volent, Z., DeCew, J., Rosten, T., Strand, I., 2015. Drag forces on, and deformation of, closed flexible bags. J. Offshore Mech. Arctic Eng. 137 (4), 041202–041202–8.

Lader, P., Fredriksson, D.W., Volent, Z., DeCew, J., Rosten, T., Strand, I., 2017. Wave response of closed flexible bags. J. Offshore Mech. Arctic Eng. 139 (5), 051301–051301–9.

Liang, H., Santo, H., Shao, Y.L., Law, Y.Z., Chan, E.S., 2020. Liquid sloshing in an upright circular tank under periodic and transient excitations. Physical Review Fluids 5, 084801.

Lukovsky, I.A., 1990. Introduction to Nonlinear Dynamics of a Solid Body with a Cavity Including a Liquid. Kiev: Naukova dumka (in Russian).

Løland, G., 1994. Fabric as construction material for marine applications. In: Proc. International Conference on Hydroelasticity in Marine Technolgy, Trondheim, Norway.

Newman, J.N., 1974. Second-order, slowly-varying forces on vessels in irregular waves. In: Proc. 1st International Symposium on Dynamics of Marine Vehicles and Structures in Waves, London, UK.

Newman, J.N., 2005. Wave effects on vessels with internal tanks. In: Proc. 20th International Workshop on Water Waves and Floating Bodies, Longyearbyen, Norway.

Pérez, T., Fossen, T.I., 2008. Time- vs. frequency-domain identification of parametric radiation force models for marine structures at zero speed. Model. Ident. Contr. 29 (1), 1–19.

Reite, K.J., Føre, M., Aarsæther, K.G., Jensen, J., Rundtop, P., Kyllingstad, L.T., Endresen, P.C., Kristiansen, D., Johansen, V., Fredheim, A., 2014. FhSim - time domain simulation of marine systems. In: Proc. 33rd International Conference on Ocean, Offshore and Arctic Engineering, San Francisco (OMAE 2014).

Royon-Lebeaud, A., Hopfinger, E.J., Cartellier, A., 2007. Liquid sloshing and wave breaking in circular and square-base cylindrical containers. J. Fluid Mech. 577, 467–494.

Shao, Y.L., Faltinsen, O.M., 2014. A harmonic polynomial cell (HPC) method for 3D Laplace equation with application in marine hydrodynamics. J. Comput. Phys. 274, 312–332.

Shen, Y.G., Firoozkoohi, R., Greco, M., Faltinsen, O.M., 2021. Experimental investigation of a closed vertical cylinder-shaped fish cage in waves. Under review for Ocean Engineering.

Solaas, F., Rudi, H., Berg, A., Tvinnereim, K., 1993. Floating fish farms with bag pens. In: Fish Farming Technology. CRC Press.

Strand, I.M., Sørensen, A., Volent, Z., Lader, P., 2016. Experimental study of current forces and deformations on a half ellipsoidal closed flexible fish cage. J. Fluid Struct. 65, 108–120.

Strand, I.M., Faltinsen, O.M., 2019. Linear wave response of a 2D closed flexible fish cage. J. Fluid Struct. 87, 58–83.

Strand, I.M., Faltinsen, O.M., 2020. Linear wave-induced dynamic structural stress analysis of a 2D semi-flexible closed fish cage. J. Fluid Struct. 94, 102909.

Su, B., Reite, K.J., Føre, M., Aarsæther, K.G., Alver, M.O., Endresen, P.C., Kristiansen, D., Haugen, J., Caharija, W., Tsarau, A., 2019. A multipurpose framework for modelling and simulation of marine aquaculture systems. In: Proc. 38th International Conference on Ocean, Offshore and Arctic Engineering, Glasgow (OMAE 2019).

Taghipour, R., Perez, T., Moan, T., 2008. Hybrid frequency–time domain models for dynamic response analysis of marine structures. Ocean Eng. 35 (7), 685–705.

Tan, Y., Shao, Y., Read, R., 2019. Coupled motion and sloshing analysis of a rigid cylindrical closed fish cage in regular waves. In: Proc. 38th International Conference on Ocean, Offshore and Arctic Engineering, Glasgow (OMAE 2019).

Tsarau, A., Lugni, C., Lucarelli, A., Kristiansen, D., Lader, P., 2021. Sloshing in a rotating liquid inside a closed sea cage for fish farming. Phys. Fluids 33, 037114.

Yu, Z., Falnes, J., 1995. State-space modelling of a vertical cylinder in heave. Appl. Ocean Res. 17, 265–275.